

Modulation of Spin Polarization and Magnetic Ordering in $\text{MSe}_2/\text{WSe}_2$ (M= 3d Transition Metal Atom) Structure: A First-Principles Study

Paras Poswal, Sheshamani Singh, Astha Suman, Rohit Kumar, and Neeraj Shukla*



Cite This: <https://doi.org/10.1021/acs.jpcc.5c01543>



Read Online

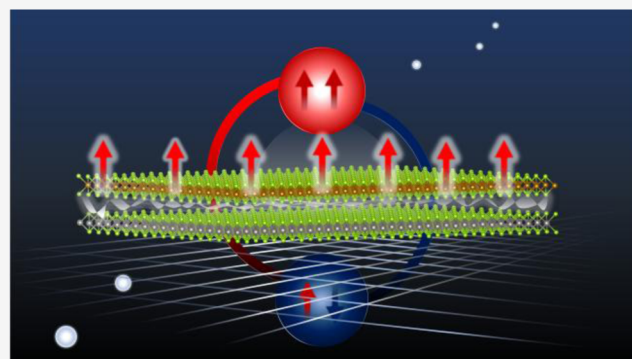
ACCESS |

Metrics & More

Article Recommendations

Supporting Information

ABSTRACT: The ability to tailor the electronic and magnetic properties of two-dimensional (2D) materials opens new avenues for designing spintronic devices. In this study, first-principles calculations have been performed to investigate the structural, electronic, and magnetic properties of bilayer tungsten diselenide (WSe_2) doped with a 3d transition metal atom. Among the two different stacking configurations considered (AA and AA') for bilayer WSe_2 , the AA' stacking configuration has been identified as energetically favorable and dynamically stable. Doping one layer of the bilayer system $\text{MSe}_2/\text{WSe}_2$ (M = Sc, Ti, V, Cr, Mn, Fe, Co, Ni, and Cu) significantly alters the electronic structures and induces finite magnetic ordering in the structures. The doped atom exhibits strong binding with neighboring Se atoms, having binding energies ranging from -2.73 eV to -6.36 eV, confirming robust structural stability. The Mn-doped structure attains a maximum magnetic moment of $3.63 \mu_B$ in its ferromagnetic state, though its antiferromagnetic state is energetically more favorable. Strain engineering further enhances the magnetic moment in the Mn-doped structure to $4.00 \mu_B$, highlighting the tunability of the system. On the other hand, the Cr-doped structure exhibits ferromagnetic ordering in its ground state with a magnetic moment of $2.48 \mu_B$. Utilizing the modified mean-field theory and Heisenberg model, the maximum Curie temperature has been approximated as 159.94 K for the $\text{CoSe}_2/\text{WSe}_2$ configuration, while the maximum Néel's temperature is estimated to be 367.67 K for the $\text{FeSe}_2/\text{WSe}_2$ configuration. The findings of this work establish a strong theoretical foundation for designing 2D materials with tunable magnetic properties, paving the way for further experimental exploration and next-generation spintronic device applications.



1. INTRODUCTION

Two dimensional (2D) materials have revolutionized the field of materials science due to their unique properties compared to their bulk counterparts.¹ Since the discovery of graphene, the first 2D material, in 2004 by Novoselov et al.,² a wide range of 2D materials have been explored, including transition metal dichalcogenides (TMDs),³ silicene,⁴ hexagonal boron nitride (h-BN),⁵ germanene,⁶ phosphorene,⁷ stanene,⁸ borophene,⁹ and MXene.¹⁰ These 2D materials have been widely studied by researchers due to their exceptional electronic, optical, mechanical, and magnetic properties, which make them highly valuable for their potential applications in next-generation electronics, optics, and spintronic devices.

The experimental realization of magnetic ordering in 2D materials like CrI_3 ,¹¹ VSe_2 ,¹² and CrGeTe_3 ¹³ has sparked great interest in the scientific community to explore 2D materials for spintronics,¹⁴ valleytronics,¹⁵ magnetic switching,^{16,17} and memory-device¹⁸ applications. Extensive theoretical and experimental studies have been conducted to reveal new magnetic materials with a fortified stability. It has been observed that doping, defects, surface functionalization, and

strain can alter the magnetic ordering in 2D materials.¹⁹ Among all these techniques, doping 2D materials with 3d TM atoms, e.g., doped TMDs,²⁰ borophenes,²¹ graphene,²² etc., have attracted great attention due to the precise control on the induced magnetic ordering.

Within this extensive range of 2D materials, TMDs have attracted considerable interest due to their robust stability and excellent performance in demanding applications. TMDs fall under the category of van der Waals (vdW) materials having strong covalent bonds within layers forming sandwich-like compositions “X–M–X” (M = TM and X = Chalcogen) with weak interlayer vdW interaction. In the chalcogen group, heavier chalcogens exhibit superior electrical conductivity, which is crucial for optoelectronics, energy-storage, and

Received: March 6, 2025

Revised: May 18, 2025

Accepted: June 5, 2025

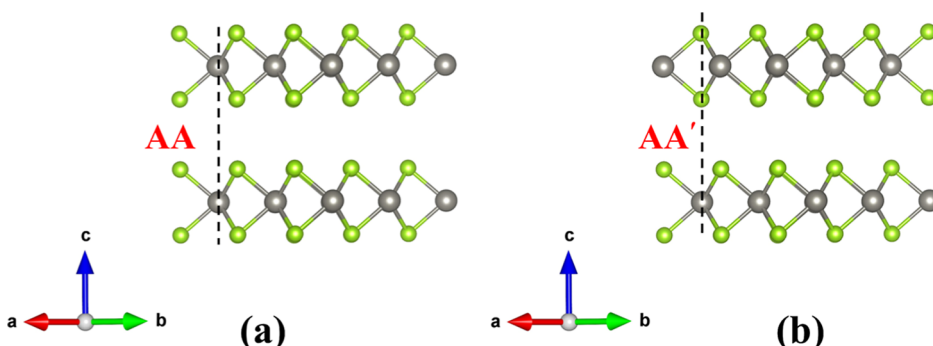


Figure 1. Stacking sequences of WSe₂ bilayers (a) AA configuration and (b) AA' configuration.

magnetic applications. Selenium (Se) is a promising candidate among the chalcogens due to its cost-effectiveness and superior electrical conductivity. TMDs consist of a wide variety of materials, and extensive work has been done on them, including MoS₂,²³ WS₂,²⁴ etc. Tungsten diselenide (WSe₂)²⁵ is another member of the TMDs family, which has attracted considerable interest due to its utilization in photodetectors,²⁶ field-effect transistors (FETs),²⁷ etc. One of the distinguished properties of WSe₂ is its strong spin-orbit coupling (SOC) compared to other TMDs. This strong SOC in WSe₂ leads to spin-orbit splitting in the conduction band (CB) as well as in the valence band (VB), which allows them to control the electron spin, making it a promising candidate for spintronic applications.²⁸ In addition to this, many research groups across the globe have been focusing to use the monolayer TMD for valleytronics applications because the crystal structure of the TMD has no inversion center, which allows for the acquisition of a new degree of freedom of charge carriers known as the k-valley index.²⁹ The realization of magnetic skyrmions and topological phase transitions in 2D-vdW magnetic materials has sparked great interest for their possible use in applications in memristive devices and neuromorphic computing.

While monolayer TMDs have demonstrated remarkable properties, recent research focus has been shifted toward their bilayer configurations and heterostructures.^{30,31} These configurations, consisting of layers of different 2D materials, including TMDs or other 2D materials, exhibit enhanced and tunable electrical properties and have made notable progress in recent years.³² The weak vdW interaction allows for flexibility in the synthesis of vdW heterostructures through artificial stacking or epitaxial growth. The unique properties, such as ultrafast charge transfer,³³ moiré excitons in twisted heterostructure,³⁴ and ultrahigh on-current and mobility,³⁵ make them highly promising for further spintronic applications.

Recently, extensive studies on bilayer WSe₂ have been conducted to modify the electronic and magnetic properties, such as achieving half-metallicity and significant spin polarization through interlayer doping with Cr, Mn, Fe, and Co.³⁶ However, inducing magnetism in bilayer WSe₂, particularly for configurations with diverse dopants and strain, is still less explored.³⁷ In this work, we fully doped one layer of W with 3d TM atoms to create MSe₂/WSe₂ configuration (where M = Sc, Ti, V, Cr, Mn, Fe, Co, Ni, and Cu) and investigated the relative changes in structural, electronic, and magnetic properties. Additionally, we explored the tunability of magnetic ordering with strain. The tunable magnetic properties in various doped structures, exhibiting ferromagnetic (FM) and

antiferromagnetic (AFM) ordering, provide a strong foundation for further experimental exploration of low-dimensional spintronic device applications.

2. COMPUTATIONAL METHODS AND DETAILS

In the present work, the electronic and magnetic properties of the MSe₂/WSe₂ bilayer configuration have been investigated utilizing the open-source computational package Quantum ESPRESSO,³⁸ which is based on first-principles (ab initio)-based density functional theory. The interaction between electrons is characterized by the generalized gradient approximation (GGA) with Perdew–Burke–Ernzerhof (PBE)³⁹ exchange functional. The interaction between ions and core electrons has been considered utilizing an ultrasoft pseudopotential. The Hubbard correction (DFT + U) has been utilized to capture the on-site Coulomb interactions of 3d TM electrons. The U-values for TMs have been estimated utilizing the linear response method.⁴⁰ A standard DFT calculation of MSe₂/WSe₂ structure with some initial guess of U values has been performed to extract the information on unperturbed Kohn–Sham wave functions and ground state spin charge density. The extracted information is then applied as input for linear response calculation for the estimation of U-values. To account for the vdW interaction between layers, we have performed all calculations with the Grimme DFT + D3 correction. Spin-polarized calculations have been performed to determine the electronic and magnetic properties. The bilayer MSe₂/WSe₂ configuration was achieved by introducing a 20 Å vacuum along the z-axis, perpendicular to the structure, which eliminates the possibility of interaction beyond the bilayer. An energy cutoff for charge density has been set to 560 Ry. A 6 × 6 × 1 Monkhorst–Pack⁴¹ k-point mesh has been utilized for the structure optimization, and all the structures have been optimized until the force on each atom is less than 10⁻⁵ Ry/Bohr. The SCF calculations have been performed with dense 12 × 12 × 1 Monkhorst–Pack k-point mesh with a total energy convergence threshold of 10⁻⁹ Ry. A unit cell containing six atoms has been considered for doping the TM atom, where TM has replaced the tungsten atom in one layer, making the structure MSe₂/WSe₂ with M = Sc, Ti, V, Cr, Mn, Fe, Co, Ni, and Cu. To examine the dynamical stability of the structure, phonon dispersion calculations have been performed utilizing the direct force-constant method implemented in the Phonopy code. The Curie/Neel's temperatures have been calculated utilizing mean-field theory approximation, with a modified coefficient optimized by Monte Carlo (MC) simulation. The Bader charge analysis^{42–45} has been performed to study the charge redistribution in doped and undoped

structure. The spin density difference between up-spin and down-spin has been estimated utilizing a postprocessing script in quantum espresso, which extracts the information from the charge density file generated after the SCF run. Packages such as VESTA⁴⁶ and XCrySDen⁴⁷ have been employed for structure visualization and acquisition of spin distribution plots.

3. RESULTS

3.1. Structural and Electronic Properties of Monolayer and Bilayer WSe₂. The structural stability of bilayer WSe₂ was investigated in detail. Based on monolayer WSe₂, two different stacking sequences have been considered for the bilayer arrangement. The two most common stacking sequences for TMDs, AA (W over W) and AA' (W over Se), are shown in Figure 1a,b, respectively.

From the ground state energy (E_g) calculations, it is established that $E_{g(AA)} > E_{g(AA')}$, which concludes that the AA' stacking configuration is energetically more favorable as compared to the AA stacking configuration. The calculated lattice parameter, interlayer distance, and formation energy for both the stacking configurations are displayed in Table S1. A more negative formation energy, as displayed in Table S1, also elucidates that the AA' stacking configuration is experimentally more favorable. The more negative formation energy of bilayer WSe₂ structures as compared to the monolayer WSe₂ structure indicates enhanced structural stability with increasing layer number. To further investigate the dynamical stability of the most favorable stacking configuration (AA'), the phonon calculation has been performed. The calculated phonon band diagram and phonon density of states (DOS) are shown in Figure S1a,b. The absence of an imaginary frequency in the phonon band diagram also confirms that the AA' stacking configuration is dynamically more stable. Thus, the AA' stacking configuration has been considered for all further investigations based on its structural and dynamical stability.

To investigate the electronic and magnetic properties, the calculated electronic band diagram and (DOS) plot of monolayer and bilayer WSe₂ are shown in Figure S2. The bilayer WSe₂ exhibits semiconductor behavior with an indirect band gap of 1.34 eV between the Γ and Λ points of VB and CB, which is 0.21 eV less as compared to monolayer WSe₂, which has a direct band gap of 1.55 eV, as shown in Figure S2b,e, respectively. In monolayer WSe₂, both CB minimum (CBM) and VB maximum (VBM) lie at the K -point due to the SOC effect. The SOC effect results in energy splitting at the K -point of the VB. In bilayer WSe₂, the interlayer coupling (ILC) effect dominates. The ILC effect leads to energy splitting in Γ point of the VB and Λ point of the CB. There is a rise in Γ point energy and a lowering in Λ point energy shown in the WSe₂ bilayer due to ILC. The interlayer interaction not only changes the electronic states but also enhances the stability of the structure considerably. It has been concluded from the DOS plot that bilayer and monolayer WSe₂ exhibit symmetry in spin-up and spin-down states, which indicates nonmagnetic behavior, classifying WSe₂ as a nonmagnetic semiconductor. We have fully doped one layer of WSe₂ by 3d TM elements (M = Sc, Ti, V, Cr, Mn, Fe, Co, Ni, and Cu), proposing the MSe₂/WSe₂ structure, to explore the possibility of magnetic ordering in bilayer configuration.

3.2. The Structural Stability of MSe₂/WSe₂ Structure. The calculated interlayer distance (h), bond length between W–Se and bond angle $\theta_{Se-W-Se}$ are 3.15, 2.54, and 83.15°,

respectively. The 3d TM atom doping in WSe₂ causes significant changes in the bond length and bond angle, resulting in an increased interlayer distance. The calculated bond length between M–Se (d_{M-Se}) and W–Se (d_{W-Se}) atoms from both layers, along with their respective bond angles $\theta_{Se-M-Se}$ and $\theta_{Se-W-Se}$ and interlayer distances (h) for various dopants (M = Sc to Cu), are shown in Table 1. All of the

Table 1. Structural Parameters Including Interlayer Spacing (h), Bond Length (d), and Bond Angle (θ) of Pristine and 3d Transition Metal Atom (M)-Doped MSe₂/WSe₂ Structures

dopants (M)	h (Å)	d_{M-Se} (Å)	d_{W-Se} (Å)	$\theta_{Se-M-Se}$ (deg)	$\theta_{Se-W-Se}$ (deg)
pristine	3.15		2.54		83.15
Sc	3.23	2.70	2.56	86.83	79.60
Ti	3.20	2.56	2.56	79.57	79.51
V	3.22	2.60	2.55	85.21	81.77
Cr	3.17	2.43	2.53	85.94	82.04
Mn	3.27	2.44	2.54	86.55	81.79
Fe	3.20	2.41	2.54	76.83	81.69
Co	3.23	2.47	2.55	76.15	81.06
Ni	3.25	2.47	2.54	82.44	82.71
Cu	3.27	2.52	2.54	82.40	83.45

structural parameters have been extracted from the optimized structure by considering the Hubbard U correction with spin-polarized calculations. The values of the Hubbard parameter U, calculated utilizing the linear-response method, are exhibited in Table 2. Doping also significantly affects the

Table 2. Hubbard Value, Binding Energy (E_b), Formation Energy ($E_{formation}$), Charge Transfer and Magnetic Moment of Isolated ($M_{isolated}$), and 3d Transition Metal Atom-Doped (M_{total}) MSe₂/WSe₂ Structures

dopants (M)	U (eV)	E_b (eV)	$E_{formation}$ (eV)	charge transfer (e)	magnetization	
					$M_{isolated}$ (μ_B)	M_{total} (μ_B)
Sc	3.19	-6.09	-16.68	1.66	1[3d ¹ 4s ²]	0.00
Ti	4.16	-6.36	-16.96	1.61	2[3d ² 4s ²]	0.00
V	5.08	-3.90	-14.49	1.18	3[3d ³ 4s ²]	2.20
Cr	6.42	-3.35	-13.95	0.98	6[3d ⁵ 4s ¹]	2.85
Mn	5.22	-3.80	-14.39	1.02	5[3d ⁵ 4s ²]	3.63
Fe	3.53	-4.20	-14.79	0.81	4[3d ⁶ 4s ²]	3.29
Co	6.58	-2.85	-13.45	0.50	3[3d ⁷ 4s ²]	1.33
Ni	9.04	-2.79	-13.39	0.58	2[3d ⁸ 4s ²]	0.70
Cu	9.33	-2.80	-13.39	0.29	1[3d ¹⁰ 4s ¹]	0.00

stability and electronic and magnetic properties of the bilayer structure, due to slight changes in the structural parameters. The structural stability of MSe₂/WSe₂ structures has been ascertained by the estimation of formation energy ($E_{formation}$) calculation, which is assessed by the following equation.

$$E_{formation} = E_{doped} - E_{TM} - nE_W - mE_{Se} \quad (1)$$

where E_{doped} is the total energy of the doped MSe₂/WSe₂ structure, E_{TM} , E_W , and E_{Se} are the total energies of the isolated 3d TM atom, W, and Se atom, respectively, and n and m are the number of W and Se atoms, respectively. The formation energies of all 3d TM-doped structures are found to be

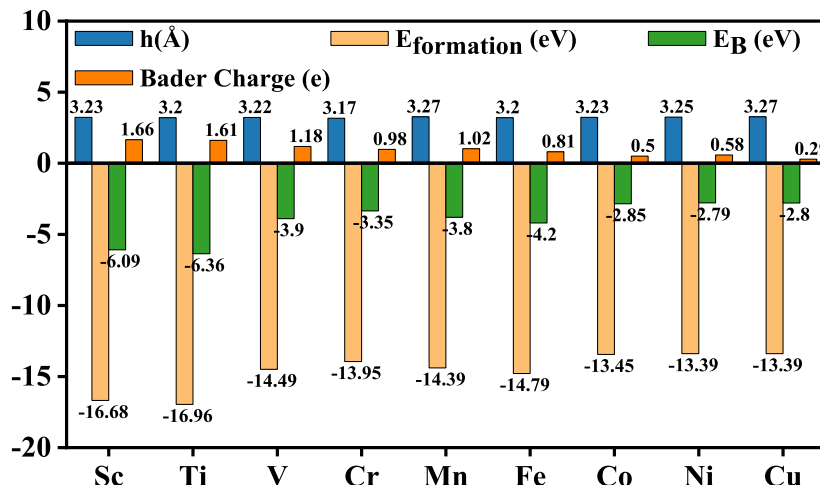


Figure 2. The graphical representation of interlayer spacing (h), the binding energy (E_b) of 3d transition metal atom-doped $\text{MSe}_2/\text{WSe}_2$ structures, formation energy ($E_{\text{formation}}$) of doped structure, and charge transfer from doped atom to structure.

negative, ranging from -13.32 eV to -16.96 eV , as shown in **Table 2**, enunciating the possibility of their potential experimental realization to a reasonable degree. The binding energy of the doped atom has also been calculated by utilizing the following equation to quantify the bonding strength between the dopant and the structure.

$$E_b = E_{\text{doped}} - E_{\text{M-vacancy}} - E_{\text{TM}} \quad (2)$$

where E_{doped} is the total energy of the doped $\text{MSe}_2/\text{WSe}_2$ structure, $E_{\text{M-vacancy}}$ is the total energy of the structure having M vacancy, and E_{TM} is the total energy of the isolated TM atom. The calculated binding energies are displayed in **Table 2**, where the more negative binding energies reveal that all the doped TM atoms make strong bonds with the neighboring atoms in $\text{MSe}_2/\text{WSe}_2$ structures. This enhanced bonding corroborates well with the respective negative structural formation energies. To further explore the interaction of doped atoms with nearest atoms, the Bader charge analysis has been performed to quantify the charge transfer. After doping, charge has been transferred from the 3d TM atom to the structure, and the calculated value of transferred charge is shown in **Table 2**. A graphical representation of interlayer spacing, formation energy, binding energy, and charge transfer for all 3d TM-doped structures is displayed in **Figure 2**. It can be observed from the comparative analysis of **Figure 2** and **Table 2**, that the dopant with a lower atomic number results in higher charge transfer. The binding energy and structural formation energy values exhibit higher negative values for lower atomic numbers and vice versa.

3.3. Electronic and Magnetic Properties of $\text{MSe}_2-\text{WSe}_2$ Structure. In this section, we investigate the potential of magnetic ordering in doped $\text{MSe}_2/\text{WSe}_2$ structures (where M = Sc, Ti, V, Cr, Mn, Fe, Co, Ni, and Cu). The calculated parameters, such as magnetic moment and relative charge transfer, are displayed in **Table 2**. The magnetic ordering in the doped system can be attributed to the 3d TM atom dopant. It can be observed from **Table 2** that only certain 3d TM-doped structures exhibit finite magnetization, e.g., V-, Cr-, Mn-, Fe-, Co-, and Ni-doped structures. The absence of finite magnetization in the case of Sc-, Ti-, and Cu-doped systems can be attributed to the unavailability of unpaired electrons. **Figure 3** reveals the variation in magnetic moments of isolated 3d TM atoms and doped $\text{MSe}_2/\text{WSe}_2$ structures. The magnetic

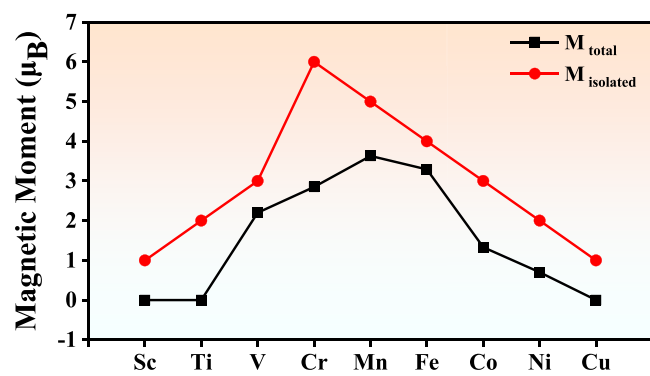


Figure 3. Magnetic moment (M_{isolated}) of isolated 3d transition metal atom and (M_{total}) of 3d transition metal atom-doped $\text{MSe}_2/\text{WSe}_2$ structures.

behavior of the $\text{MSe}_2/\text{WSe}_2$ structure is determined by the interaction of the localized 3d-orbitals of the dopant atoms with the p-orbitals of the surrounding Se atoms. For isolated 3d TM atoms, the magnetic moment originates from unpaired electrons. However, in the present case of interacting 3d TM atom dopants, the magnetic moment is altered due to crystal field splitting, hybridization, and charge transfer. For elements like Mn and Fe, small charge transfer and hybridization stabilize the high-spin states, resulting in maximum magnetic ordering. However, dopants Sc and Ti exhibit complete quenching of magnetic moment. It has been observed from **Table 2** that magnetic moments start increasing beyond the dopant Ti and attain a maximum value of $3.63 \mu_B$ in the Mn-doped structure, and after that it gradually decreases for other dopants with increasing Z value. Strong hybridization with the host material's orbitals can delocalize d-electrons, reducing the total magnetic moment (M_{total}). Isolated Mn ($3d^5, 4s^2$) atom has five unpaired electrons in the d-orbital, and after doping, a 1.02 e charge is transferred from Mn to the structure. Charge transfer between the dopant and the structure further modifies the spin density by altering electron occupation in spin-up and spin-down states. The magnetic moment of the Mn-doped structure has been further altered by strain modulation, as shown in **Table 3**.

Here the compressive and tensile biaxial strain, ranging from -10% to 10% , has been applied to the structure, which

Table 3. Effect of Biaxial Strain on Magnetic Moment (M_{total}) and Distance between Dopant (Mn) $d_{\text{TM-TM}}$ of $\text{MnSe}_2/\text{WSe}_2$ Structures

strain (%)	-10	-7.5	-5.0	-2.5	0.0	2.5	5.0	7.5	10
$M_{\text{total}} (\mu_B)$	4.00	3.87	3.77	3.67	3.63	3.62	3.53	3.44	3.23
$d_{\text{TM-TM}} (\text{\AA})$	3.01	3.09	3.17	3.25	3.34	3.42	3.51	3.59	3.67

influences the atomic position and resultant magnetic moment. As displayed in Figure 4, on applying compressive strain

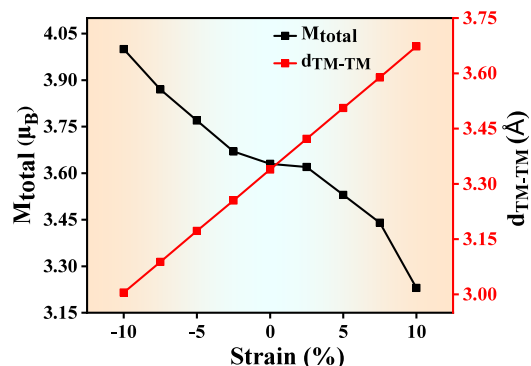


Figure 4. Strain-dependent magnetic moment (M_{total}) and distance between dopant (Mn) of $\text{MnSe}_2/\text{WSe}_2$ structures.

(0%–10%) on the Mn-doped structure, the magnetic moment value enhances from $3.63 \mu_B$ to $4.00 \mu_B$. The applied compressive strain (0%–10%) changes the distance between the doped atoms, reducing it from 3.339\AA to 3.005\AA , which enhances the strength of magnetic exchange interaction responsible for increased magnetic ordering.

To gain deeper insights into the spin distribution, we have calculated the spin density difference ($\rho_{\text{up}} - \rho_{\text{down}}$). Figure 5

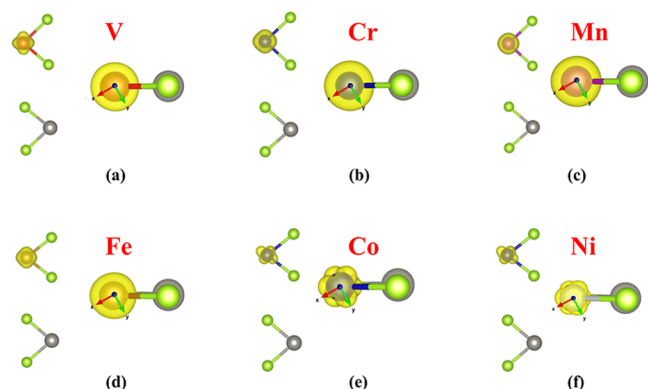


Figure 5. Spin density ($\rho_{\text{up}} - \rho_{\text{down}}$) isosurface for (a) V-, (b) Cr-, (c) Mn-, (d) Fe-, (e) Co-, and (f) Ni-doped $\text{MSe}_2/\text{WSe}_2$ structures having isosurface value 0.042.

exhibits the spin density difference isosurface of doped structures in both the side and top views. The results reveal that the finite spin density difference is predominantly located around the doped 3d TM atom. This elucidates that the origin of magnetism in the doped structure is mostly attributed to the 3d TM atom. A nonuniform distribution of spin density difference has been found near the doped atom. This happens due to the uneven distribution of spin-up and spin-down electrons in d_{xy} , d_{yz} , d_{zx} , $d_{x^2-y^2}$, and d_{z^2} orbitals of the doped atom.

The DOS, including the total DOS (TDOS) and partial DOS (PDOS), have been calculated to further explore the orbital contribution and understand the origin of magnetism in the doped structure, as displayed in Figure 6a–l. The total DOS with doped TM atom's 3d-orbital, Se's p-orbital, and W's 4d-orbital is shown in Figure 6a–f, and their respective 3d orbitals are divided into E_1 (d_{xz} , d_{yz}), E_2 (d_{xy} , $d_{x^2-y^2}$), and A_1 (d_{z^2}) orbitals, as shown in Figure 6g–l. $\text{MnSe}_2/\text{WSe}_2$ structures exhibit the highest magnetization due to higher asymmetry in spin-up and spin-down channels in the TDOS and PDOS, as shown in Figure 6c,I, respectively. The majority spin states in the 3d orbital of Mn are found in the VB, while minority spin states are found in the CB, due to redistribution of electrons. After the redistribution, the A_1 , E_1 , and E_2 states of Mn dominate the spin-up states, while the A_1 and E_2 states dominate the spin-down states. The reduction of unpaired electron from the Mn 3d orbital is due to the interaction of the Mn 3d orbital with the Se p-orbital, which reduces the net magnetic moment of the Mn-doped structure as compared to its isolated counterpart. Spin-up electrons in 3d orbital of V- and Cr-doped systems majoritarily contribute to magnetism, where the spin-up states near the Fermi level are contributed by A_1 and E_2 states of 3d orbitals, while electrons in spin-down states are occupied by the E_1 state near the Fermi level.

A noticeable and steady spin-down state contribution has been found due to the increase of electrons in the 3d orbital, for Fe, Co, and Ni dopants, beyond Mn. This increases the number of paired electrons in the system, resulting in reduced magnetic ordering.

The doping of TM atoms not only changes the magnetic properties but also alters the electronic properties of $\text{MSe}_2/\text{WSe}_2$ structures. The electronic band structure calculation has been performed to identify the changes in electronic state, post doping. The pristine WSe_2 bilayer exhibits semiconducting nature with indirect band gap, as shown in Figure S2e. The doping of TM at the W site changes the electronic state from semiconducting to metallic, as depicted in the electronic band diagram of spin-up and spin-down states in Figure 7a–f. After doping, some new states arise near the Fermi level due to 3d orbitals of the doped TM atom. These emergent states overlap with the CB and VB of the WSe_2 , making $\text{MSe}_2/\text{WSe}_2$ structures metallic. Doping also alters the ILC, which results in significant changes in undoped WSe_2 layer's structure parameters, including bond length and bond angle, as elucidated in Table 1. These structural changes and ILC effects alter the band structure of WSe_2 . The spin-up and spin-down bands, exhibit different electronic configurations, due to the different distributions of spin-up and spin-down electrons in 3d orbital. For V-, Cr-, and Mn-doped structures, the bands in the spin-up state cross the Fermi level, but spin-down bands exhibit an energy gap inside CB, which can be further modulated by external perturbations, e.g., electric field, strain, etc. This opens up the possibility for V-, Cr-, and Mn-doped structures to be utilized in spin filtration applications by shifting the gap toward the Fermi level. For Fe-, Co-, and Ni-doped structures, the electrons found in spin-up and spin-

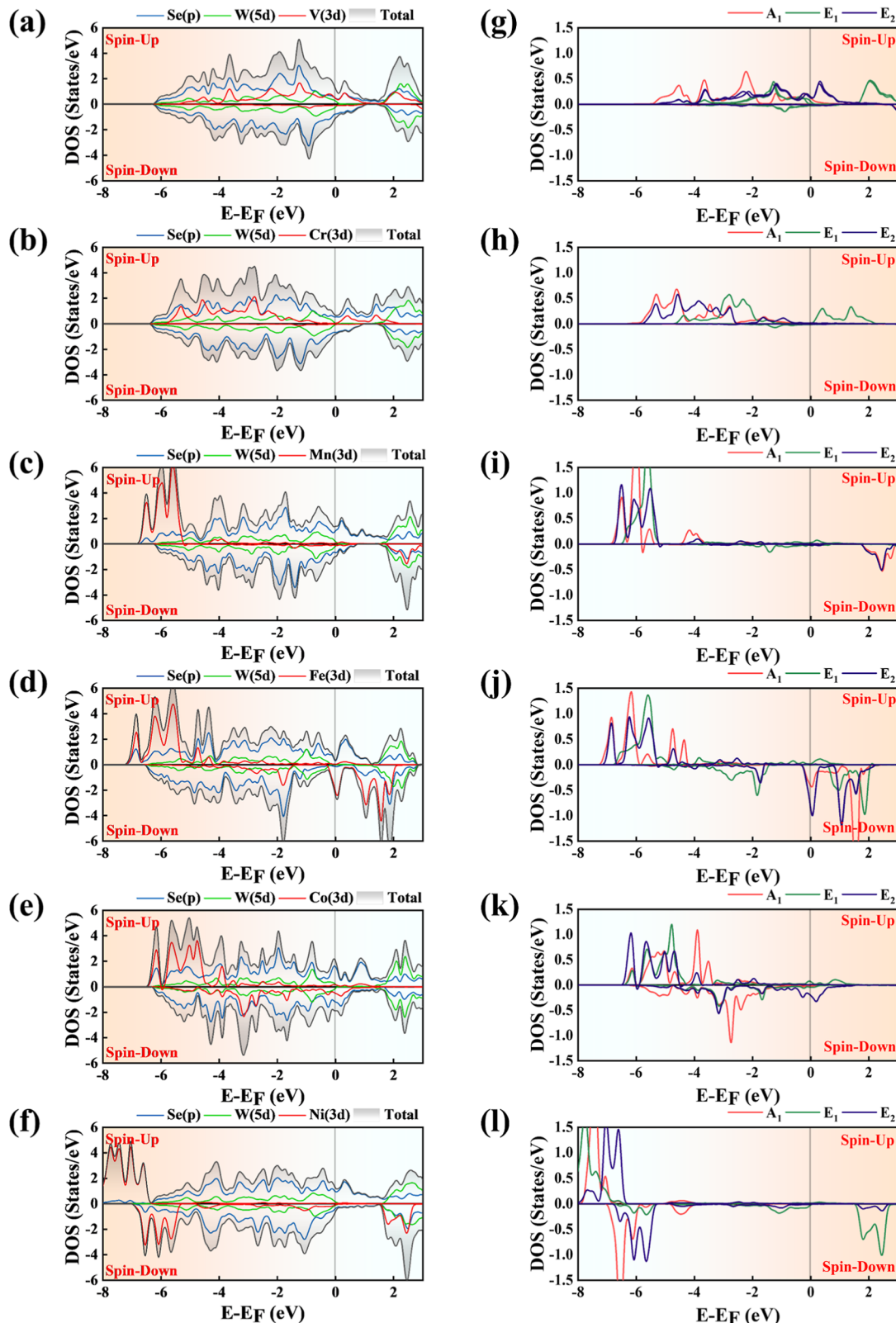


Figure 6. Partial density of states (PDOS) of (a) V_x, (b) Cr_x, (c) Mn_x, (d) Fe_x, (e) Co_x, and (f) Ni-doped MSe₂-WSe₂ structures and the contribution of 3d orbital divided into E₁ (d_{xz} , d_{yz}), E₂ (d_{xy} , $d_{x^2-y^2}$), and A₁ (d_z^2) orbitals from (g) to (l), respectively.

down states, create enough electronic population at the Fermi level to make the system completely metallic. These band characteristics corroborate well with the DOS results shown in Figure 6a–l.

3.4. Degree of Spin Polarization. It has been observed from the DOS and PDOS of MSe₂/WSe₂ structures, as shown in Figure 6a–f, that, in some cases, the density for spin-up and spin-down states, varying significantly due to the redistribution of electrons at the Fermi level. From the total DOS, we have

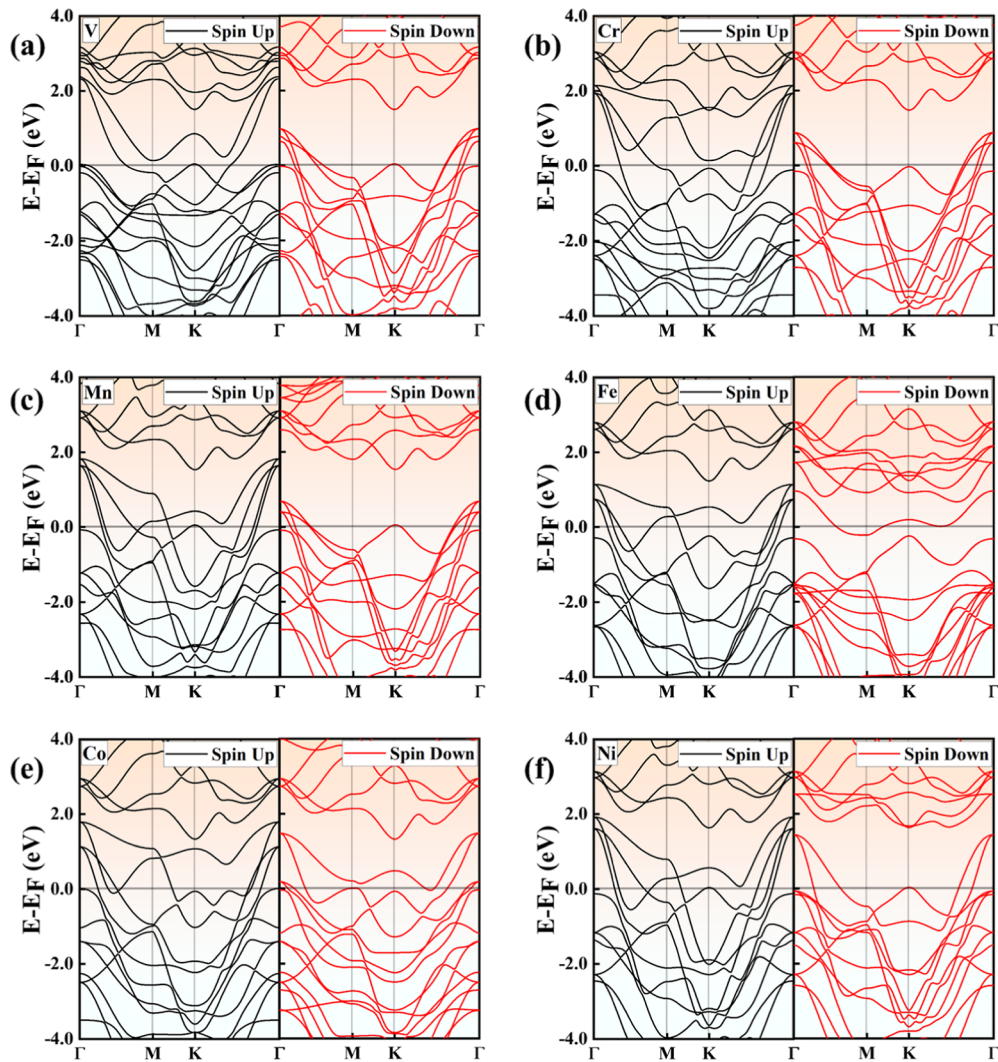


Figure 7. The band diagram of transition metal-doped MSe₂/WSe₂ structures (a) VSe₂/WSe₂ structure, (b) CrSe₂/WSe₂ structure, (c) MnSe₂/WSe₂ structure, (d) FeSe₂/WSe₂ structure, (e) CoSe₂/WSe₂ structure, and (f) NiSe₂/WSe₂ structure.

calculated the degree of spin polarization to identify the contribution of spin states. Soulent Jr. et al.⁴⁸ in their work related to the quantitative analysis of the degree of polarization, have suggested that the degree of spin polarization in a material at Fermi level (E_F), can be calculated by utilizing the following equation

$$P = \frac{N_{\uparrow}(E_F) - N_{\downarrow}(E_F)}{N_{\uparrow}(E_F) + N_{\downarrow}(E_F)} \times 100\% \quad (3)$$

where $N_{\uparrow}(E_F)$ and $N_{\downarrow}(E_F)$ can be found from the DOS of the spin-up and spin-down states at the Fermi level. The calculated values of degree of spin polarization (P) for MSe₂/WSe₂ structures having finite magnetic ordering are displayed in Table 4. The Fe-doped structure shows a higher degree of spin polarization value (−75%), where the negative sign indicates that the spin-down state is highly populated at the Fermi level as compared to the spin-up state. The maximum degree of spin polarization (34.80%) for the spin-up case has been found in the Ni-doped structure. Relatively less degree of spin polarization has been found in the case of V-, Cr-, Mn-, and Co-doped structures. The variation in degree of spin polarization for different dopants is due to the intrinsic electronic structure of the dopant and its hybridization with

Table 4. Degree of Spin Polarization with Spin-Up and Spin-Down States at Fermi Level for MSe₂/WSe₂ Structures

dopants (M)	$N_{\uparrow}(E_F)$	$N_{\downarrow}(E_F)$	P (%)
V	1.21	1.1	4.76
Cr	0.66	0.81	−10.20
Mn	1.38	0.98	16.94
Fe	0.35	2.45	−75.00
Co	2.02	1.89	3.32
Ni	1.22	0.59	34.80

the nearest Se atoms in MSe₂/WSe₂ structures. Specifically, in the CrSe₂/WSe₂ structure, the hybridization of the Cr 3d-orbital with the Se 4p-orbital, leads to the redistribution of the DOS near the Fermi level, where spin-down states dominate due to greater Se p-orbital contributions in the spin-down channel. In FeSe₂/WSe₂ structure, strong spin-down polarization has been found due to the significant contribution from the spin-down state of Fe's 3d-orbitals, particularly the E₂ (d_{xy} , $d_{x^2-y^2}$) contribution of the 3d orbital, near the Fermi level, as shown in the PDOS of the doped MSe₂/WSe₂ structure in Figure 6a–l.

3.5. Magnetic Exchange Interaction. The magnetic exchange interaction is a quantum effect that arises from the

magnetic coupling between spins. Based on the exchange interaction, parallel and antiparallel spin configurations occur in the system, which result in FM and AFM magnetic ordering, respectively. The strength of the magnetic exchange interaction is directly dependent on the exchange energy. The exchange energy can be assessed by utilizing the following equation:

$$\Delta E = E_{\text{AFM}} - E_{\text{FM}} \quad (4)$$

where (E_{AFM}) is the ground state energy of the AFM state and (E_{FM}) is the ground state energy of the FM state. The sign and magnitude of the exchange energy (ΔE) reveal the type of magnetic interaction and the stability of the resultant magnetic phase. In a doped structure, magnetism is localized near the doped atom. To account for the magnetic interaction between the nearest doped atoms, the size of supercell has been doubled in the x -direction and parallel and antiparallel spins have been assigned to both doped atoms. The exchange energy has been calculated by utilizing eq 4 and is exhibited in Table 5. It has been found that V-, Cr-, and Co-doped structures

Table 5. Exchange Energy ΔE , Magnetic Coupling, Distance between Dopant $d_{\text{TM-TM}}$, Angle between Dopant via Se ($\theta_{\text{TM-Se-TM}}$) and Curie/Neel's Temperature for $\text{MSe}_2-\text{WSe}_2$ Structures

dopants (M)	$d_{\text{TM-TM}}$ (Å)	$\theta_{\text{M-Se-M}}$ (deg)	ΔE (meV)	coupling	$T_{\text{C/N}}$ (K)
V	3.31	94.64	79.87	FM	139.02
Cr	3.33	93.89	54.12	FM	94.21
Mn	3.34	96.64	-193.09	AFM	336.11
Fe	3.34	103.07	-211.22	AFM	367.67
Co	3.36	103.84	91.89	FM	159.94
Ni	3.31	94.30	-68.39	AFM	119.04

exhibit positive exchange energy, indicating that the FM ordering is energetically more favorable. The spin of these doped atoms favors parallel alignment to minimize the total energy of the structure.

The Co-doped structure having the highest positive exchange energy shows that the magnetic interaction between Co-Co atoms is stronger as compared to other doped structures, and the structure exhibits a highly stable FM phase. Mn-, Fe-, and Ni-doped structures exhibit negative exchange energy, indicating that AFM ordering is energetically more favorable in these doped structures. The Mn-doped structure shows large negative exchange energy, which suggests that the

Mn-doped structure exhibits a stable AFM phase wherein interaction is mediated by Se atoms. The comparatively large exchange energy value in FM and AFM ordering exhibits the strength of the magnetic phase stability of the structure. The FM and AFM magnetic ordering in the $\text{MSe}_2/\text{WSe}_2$ structure is governed by the combination of several exchange interactions. A weak direct exchange is expected due to the possibility of 3d orbital overlap of the magnetic dopant. A relatively large separation (3.1–3.5 Å) between magnetic dopants, as displayed in Table 5, suggests that the direct exchange is negligible and can be ignored. The system exhibits M–Se–M bonds, with bond angles ($\theta_{\text{M-Se-M}}$) ranging from 93.89° to 103.84°, as displayed in Table 5. This structural geometry provides a pathway for superexchange interaction. According to the Goodenough-Kanamori-Anderson (GKA) rule, superexchange interaction promotes FM ordering, when the angle between magnetic atoms, mediated by a nonmagnetic atom, is around 90° and AFM ordering is more favorable when the angle approaches toward 180°.^{49,50} The $\text{CrSe}_2/\text{WSe}_2$ and $\text{VSe}_2/\text{WSe}_2$ structures with bond angles ($\theta_{\text{M-Se-M}}$) 93.89° and 94.64°, respectively, exhibit FM behavior, which aligns well with the superexchange interaction framework. The $\text{MnSe}_2/\text{WSe}_2$ and $\text{FeSe}_2/\text{WSe}_2$ structures exhibit AFM ordering, which could be elucidated as a combination of the GKA rule for larger angles and specific electron fillings in 3d orbitals.⁵¹ The metallic behavior of the $\text{MSe}_2/\text{WSe}_2$ structure further suggests that the magnetic interaction could be mediated by conduction electrons as well. This exhibits the possibility of RKKY-type interaction.^{52–54} The significant magnitude of exchange energies ranges from 54.12 meV to 211.22 meV, which indicates a more localized mechanism. Thus, RKKY-type interaction alone is insufficient to account for such strong magnetic coupling at these distances. It is therefore suggested that the dominating exchange mechanism is a hybridized form of superexchange, which may be enhanced by orbital hybridization or metallic nature. The FM ordering in $\text{CoSe}_2/\text{WSe}_2$ structure having bond angle ($\theta_{\text{M-Se-M}}$) of 104°, suggests that not only the geometry of the structures but also the orbital characteristics and hybridizations play a critical role in FM/AFM type of magnetic ordering.

3.6. Curie/Neel's Temp. The Curie/Neel's temperature is one of the essential properties in determining the thermal stability of the magnetic phase in 2D materials. While the traditional mean field theory often overestimates the Curie/Neel's temperature, a more accurate approach is the combination of mean field theory with slight modification. Y

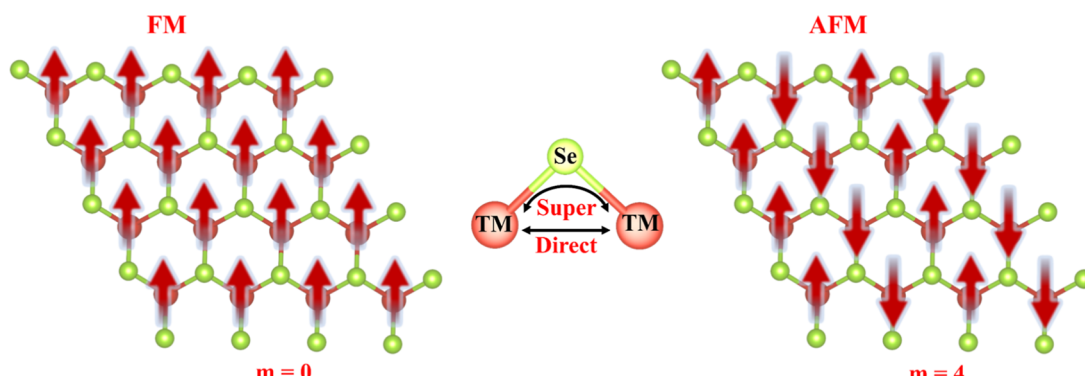


Figure 8. The ferromagnetic (FM) and antiferromagnetic (AFM) magnetic order of MSe_2 layer of $\text{MSe}_2/\text{WSe}_2$ structure with possible exchange interaction path.

Xue et al. (2022)⁵⁵ proposed an alternative formula based on the theoretical foundation of mean-field theory and MC studies, which is as follows

$$K_B T_C \approx \frac{\beta}{2m} \Delta E \quad (5)$$

where ΔE is the energy difference between AFM and FM order, the coefficient “ β ” for different lattice types are $\beta = 0.40$, 0.63 , and 1.20 for 2D honeycomb lattice, simple cubic lattice, and hexagonal close-packed lattice, respectively. In the structures MSe_2/WSe_2 , the magnetic dopants (M) have been arranged in a hexagonal closed pack structure; therefore, $\beta = 1.20$ has been considered and m is the number of neighboring antiparallel spin, which is equal to 4 , as shown in Figure 8. The calculated value of Curie/Neel's temperature utilizing modified mean field theory is shown in Table 5. The Co-doped structure having FM ordering exhibits a stable magnetic phase up to 159.94 K, while the Fe-doped structure shows Neel's temperature of 367.67 K in its favorable AFM state.

4. DISCUSSION

The doping of 3d TM atom in the top layer of WSe_2 transforms the structure into MSe_2/WSe_2 configuration, in which the top-doped layer exhibits magnetic ordering. This selective doping not only changes the magnetic properties but also transforms the electronic state from semiconducting phase having an indirect band gap of 1.34 eV into a metallic state. This change in the electronic state has been observed due to the introduction of unpaired 3d electrons into the system. These extra electrons populate new states near the Fermi level due to the hybridization of the 3d orbitals of the dopant with p-orbitals of Se, which breaks the spin symmetry. The strength of hybridization depends on the dopant's electronic configuration, bond distance, and bond angle between the dopant and surrounding atoms. Among all the doped structures, the largest magnetic moment of $3.63 \mu_B$ is observed in the Mn-doped structure, due to the presence of the maximum number of unpaired electrons. A similar finding has been reported by Tiwari et al., where they have reported high magnetic moment in Mn-doped $MoSe_2$ through DFT calculations.⁵⁶ This magnetic moment was further enhanced by applying biaxial strain. The application of biaxial strain in the MSe_2/WSe_2 structure, reveals a fascinating strain-dependent modification of magnetic properties. The magnetic moment of the Mn-doped structure enhances from $3.63 \mu_B$ at 0% of strain to $4.00 \mu_B$ under 10% of compressive strain. Under compressive biaxial strain, the lattice parameters reduce, which results in a reduction of bond lengths and an increase in orbital overlap between the 3d dopant and surrounding atoms. The enhancement in magnetic moment value under compressive strain can also be understood utilizing the Ruderman–Kittel–Kasuya–Yosida (RKKY) theory, which predicts that the strength of exchange interactions increases as the distance between magnetic atoms decreases.^{52,53} On the other hand, tensile biaxial strain increases the bond lengths, reducing orbital overlap and weakening the exchange interactions. This strain dependence magnetic moment variation offers potential for the development of strain-engineered 2D spintronic devices, facilitating the dynamic manipulation of magnetic properties for applications such as data storage, logic devices, etc. Although the Mn-doped system exhibits the highest magnetic moment in the FM state, energetically, it is favorable in the AFM state. The AFM ordering observed in this system

can be due to the superexchange interaction,⁵⁷ where indirect coupling between Mn atoms, governed by virtual electron hopping of d-shell electrons,⁵⁷ is mediated by nonmagnetic Se atoms. Apart from Mn-, Fe-, and Ni-doped structures, other structures (V-, Cr-, and Co-doped) energetically prefer FM ordering. Since all the atoms at the W site in top layers of WSe_2 have been replaced by TM dopants, the doped atoms fulfill the geometric condition to exhibit FM ordering via superexchange interaction, as per the GKA rule. The presence of the RKKY exchange interaction may also be a reality in cases where interaction is mediated by conduction electrons as the system is metallic. Charge transfer between the dopant atoms and the WSe_2 significantly contributes to the observed electronic and magnetic properties. Bader charge analysis reveals that a significant charge is transferred from the 3d TM atoms to the Se atoms, changing the local electronic structure and resulting in the hybridization of the p-orbitals of Se with the d-orbitals of the dopant. This redistribution of charges initiates spin asymmetry and leads to the spin polarization observed in the doped structures. The behavior of 3d TM doping reported in our work matches well with previous reported findings.^{56,58}

The results from this study align well with the research on TM-doped TMDs. The ability to manipulate electronic and magnetic properties through doping and strain engineering offers exciting possibilities for applications in spintronics and magnetic storage technologies. By correlating these findings with previous studies, we conclude that the MSe_2/WSe_2 structure holds great promise for next-generation stable spintronic devices, offering tunable magnetic and electronic properties that can be tailored to specific technological needs.

5. CONCLUSIONS

In this study, a detailed first-principles investigation has been conducted to explore the structural, electronic, and magnetic properties of MSe_2/WSe_2 structures. Our calculations suggest that the AA' stacking configuration of bilayer WSe_2 is dynamically stable and energetically more favorable, providing a stable platform for doping. The negative formation energy of the doped structure indicates their stability and potential for the experimental availability of these structures. All the doped structures except Sc-, Ti-, and Cu-doped, exhibit magnetic ordering. Further analysis of the magnetic exchange energy calculations reveals that the Mn-, Fe-, and Ni-doped structures display AFM ordering, whereas the V-, Cr-, and Co-doped structures exhibit FM ordering. However, the Mn-doped structure is energetically more stable in the AFM state, despite displaying a large magnetic moment of $3.63 \mu_B$ in the FM state. Strong FM coupling and a high Curie temperature of 139.02 K in the V-doped structure make VSe_2-WSe_2 an excellent candidate for spintronic applications, particularly in devices that require strong FM ordering. This work highlights the potential of doped TMDs for next-generation technologies by opening new avenues for their investigation in magnetic and spintronic device applications.

■ ASSOCIATED CONTENT

SI Supporting Information

The Supporting Information is available free of charge at <https://pubs.acs.org/doi/10.1021/acs.jpcc.5c01543>.

Structural detail, phonon band diagram, electronic band diagram, and spin-polarized density of states of WSe_2 structures (PDF)

AUTHOR INFORMATION

Corresponding Author

Neeraj Shukla — Department of Physics, National Institute of Technology Patna, Patna, Bihar 800005, India;
 ⓘ orcid.org/0000-0003-4824-3725; Email: neerajs@nitp.ac.in

Authors

Paras Poswal — Department of Physics, National Institute of Technology Patna, Patna, Bihar 800005, India;
 ⓘ orcid.org/0009-0003-5383-5538

Sheshamani Singh — Department of Physics, National Institute of Technology Patna, Patna, Bihar 800005, India

Asthya Suman — Department of Physics, National Institute of Technology Patna, Patna, Bihar 800005, India;
 ⓘ orcid.org/0009-0002-9894-5266

Rohit Kumar — Department of Physics, National Institute of Technology Patna, Patna, Bihar 800005, India

Complete contact information is available at:
<https://pubs.acs.org/10.1021/acs.jpcc.5c01543>

Author Contributions

The manuscript was prepared through contributions of all authors. All authors have given their approval to the final version of the manuscript.

Notes

The authors declare no competing financial interest.

ACKNOWLEDGMENTS

Paras Poswal acknowledges NIT Patna and the Ministry of Education (MoE) for the fellowship. We acknowledge the Department of Science and Technology (DST) and the Ministry of Electronics and IT (MeitY) for providing access to the High-Performance Computing (HPC) facility (PARAM Smriti, NABI Mohali) through the National Supercomputing Mission (NSM).

REFERENCES

- (1) Glavin, N. R.; Rao, R.; Varshney, V.; Bianco, E.; Apte, A.; Roy, A.; Ringe, E.; Ajayan, P. M. Emerging Applications of Elemental 2D Materials. *Adv. Mater.* **2020**, *32* (7), 1–22.
- (2) Novoselov, K. S.; Geim, A. K.; Morozov, S. V.; Jiang, D.; Zhang, Y.; Dubonos, S. V.; Grigorieva, I. V.; Firsov, A. A. Electric Field Effect in Atomically Thin Carbon Films. *Science* **2004**, *306* (5696), 666–669.
- (3) Manzeli, S.; Ovchinnikov, D.; Pasquier, D.; Yazyev, O. V.; Kis, A. 2D Transition Metal Dichalcogenides. *Nat. Rev. Mater.* **2017**, *2* (8), 17033.
- (4) Ju, W.; Li, T.; Su, X.; Cui, H.; Li, H. Engineering Magnetism and Electronic Properties of Silicene by Changing Adsorption Coverage. *Appl. Surf. Sci.* **2016**, *384*, 65–72.
- (5) Roy, S.; Zhang, X.; Puthirath, A. B.; Meiyazhagan, A.; Bhattacharyya, S.; Rahman, M. M.; Babu, G.; Susarla, S.; Saju, S. K.; Tran, M. K.; Sassi, L. M.; Saadi, M. A. S. R.; Lai, J.; Sahin, O.; Sajadi, S. M.; Dharmarajan, B.; Salpekar, D.; Chakingal, N.; Baburaj, A.; Shuai, X.; Adumbumkulath, A.; Miller, K. A.; Gayle, J. M.; Ajnsztajn, A.; Prasankumar, T.; Harikrishnan, V. V. J.; Ojha, V.; Kannan, H.; Khater, A. Z.; Zhu, Z.; Iyengar, S. A.; Autreto, P. A. da S.; Oliveira, E. F.; Gao, G.; Birdwell, A. G.; Neupane, M. R.; Ivanov, T. G.; Taha-Tijerina, J.; Yadav, R. M.; Arepalli, S.; Vajtai, R.; Ajayan, P. M. Structure, Properties and Applications of Two-Dimensional Hexagonal Boron Nitride. *Adv. Mater.* **2021**, *33* (44), 1–48.
- (6) Acun, A.; Zhang, L.; Bampoulis, P.; Farmanbar, M.; van Houselt, A.; Rudenko, A. N.; Lingenfelder, M.; Brocks, G.; Poelsema, B.; Katsnelson, M. I.; Zandvliet, H. J. W. Germanene: The Germanium Analogue of Graphene. *J. Phys.: Condens. Matter* **2015**, *27* (44), 443002.
- (7) Carvalho, A.; Wang, M.; Zhu, X.; Rodin, A. S.; Su, H.; Castro Neto, A. H. Phosphorene: From Theory to Applications. *Nat. Rev. Mater.* **2016**, *1* (11), 16061.
- (8) Balendhran, S.; Walia, S.; Nili, H.; Sriram, S.; Bhaskaran, M. Elemental Analogues of Graphene: Silicene, Germanene, Stanene, and Phosphorene. *Small* **2015**, *11* (6), 640–652.
- (9) Ranjan, P.; Lee, J. M.; Kumar, P.; Vinu, A. Borophene: New Sensation in Flatland. *Adv. Mater.* **2020**, *32* (34), 1–13.
- (10) Naguib, M.; Barsoum, M. W.; Gogotsi, Y. Ten Years of Progress in the Synthesis and Development of MXenes. *Adv. Mater.* **2021**, *33* (39), 1–10.
- (11) McGuire, M. A.; Dixit, H.; Cooper, V. R.; Sales, B. C. Coupling of Crystal Structure and Magnetism in the Layered, Ferromagnetic Insulator CrI₃. *Chem. Mater.* **2015**, *27* (2), 612–620.
- (12) Yu, W.; Li, J.; Herng, T. S.; Wang, Z.; Zhao, X.; Chi, X.; Fu, W.; Abdelwahab, I.; Zhou, J.; Dan, J.; Chen, Z.; Chen, Z.; Li, Z.; Lu, J.; Pennycook, S. J.; Feng, Y. P.; Ding, J.; Loh, K. P. Chemically Exfoliated VSe₂ Monolayers with Room-Temperature Ferromagnetism. *Adv. Mater.* **2019**, *31* (40), 1–8.
- (13) Gong, C.; Li, L.; Li, Z.; Ji, H.; Stern, A.; Xia, Y.; Cao, T.; Bao, W.; Wang, C.; Wang, Y.; Qiu, Z. Q.; Cava, R. J.; Louie, S. G.; Xia, J.; Zhang, X. Discovery of Intrinsic Ferromagnetism in Two-Dimensional van Der Waals Crystals. *Nature* **2017**, *546* (7657), 265–269.
- (14) Kajale, S. N.; Hanna, J.; Jang, K.; Sarkar, D. Two-Dimensional Magnetic Materials for Spintronic Applications. *Nano Res.* **2024**, *17* (2), 743–762.
- (15) Luo, C.; Huang, Z.; Qiao, H.; Qi, X.; Peng, X. Valleytronics in Two-Dimensional Magnetic Materials. *J. Phys. Mater.* **2024**, *7* (2), 022006.
- (16) Kajale, S. N.; Nguyen, T.; Chao, C. A.; Bono, D. C.; Boonkird, A.; Li, M.; Sarkar, D. Current-Induced Switching of a van Der Waals Ferromagnet at Room Temperature. *Nat. Commun.* **2024**, *15* (1), 1485.
- (17) Yan, S.; Tian, S.; Fu, Y.; Meng, F.; Li, Z.; Lei, H.; Wang, S.; Zhang, X. Highly Efficient Room-Temperature Nonvolatile Magnetic Switching by Current in Fe₃GaTe₂ Thin Flakes. *Small* **2024**, *20* (23), 2311430.
- (18) Xue, F.; Zhang, C.; Ma, Y.; Wen, Y.; He, X.; Yu, B.; Zhang, X. Integrated Memory Devices Based on 2D Materials. *Adv. Mater.* **2022**, *34* (48), 2201880.
- (19) Yu, S.; Tang, J.; Wang, Y.; Xu, F.; Li, X.; Wang, X. Recent Advances in Two-Dimensional Ferromagnetism: Strain-, Doping-, Structural- and Electric Field-Engineering toward Spintronic Applications. *Sci. Technol. Adv. Mater.* **2022**, *23* (1), 140–160.
- (20) Xia, B.; Gao, D.; Xue, D. Ferromagnetism of Two-Dimensional Transition Metal Chalcogenides: Both Theoretical and Experimental Investigations. *Nanoscale* **2021**, *13* (30), 12772–12787.
- (21) Poswal, P.; Shukla, N. Unveiling the Electronic and Magnetic Landscape of 3d Transition Metal Doped Hydrogenated Borophenes: A First-Principles Study. *Phys. Chem. Chem. Phys.* **2024**, *26* (31), 20864–20874.
- (22) Santos, E. J. G.; Ayuela, A.; Sánchez-Portal, D. First-Principles Study of Substitutional Metal Impurities in Graphene: Structural, Electronic and Magnetic Properties. *New J. Phys.* **2010**, *12* (5), 053012.
- (23) Wang, Z.; Mi, B. Environmental Applications of 2D Molybdenum Disulfide (MoS₂) Nanosheets. *Environ. Sci. Technol.* **2017**, *51* (15), 8229–8244.
- (24) Lan, C.; Li, C.; Ho, J. C.; Liu, Y. 2D WS₂: From Vapor Phase Synthesis to Device Applications. *Adv. Electron. Mater.* **2021**, *7* (7), 1–36.
- (25) Eftekhari, A. Tungsten Dichalcogenides (WS₂, WSe₂, and WTe₂): Materials Chemistry and Applications. *J. Mater. Chem. A* **2017**, *5* (35), 18299–18325.
- (26) Zheng, Z.; Zhang, T.; Yao, J.; Zhang, Y.; Xu, J.; Yang, G. Flexible, Transparent and Ultra-Broadband Photodetector Based on

- Large-Area WSe₂ Film for Wearable Devices. *Nanotechnology* **2016**, *27* (22), 225501.
- (27) Hong, S. J.; Park, M.; Kang, H.; Lee, M.; Jeong, D. H.; Park, Y. W. Fabrication and Independent Control of Patterned Polymer Gate for a Few-Layer WSe₂ Field-Effect Transistor. *AIP Adv.* **2016**, *6* (8), 085320.
- (28) Yuan, H.; Bahramy, M. S.; Morimoto, K.; Wu, S.; Nomura, K.; Yang, B.-J.; Shimotani, H.; Suzuki, R.; Toh, M.; Kloc, C.; Xu, X.; Arita, R.; Nagaosa, N.; Iwasa, Y. Zeeman-Type Spin Splitting Controlled by an Electric Field. *Nat. Phys.* **2013**, *9* (9), 563–569.
- (29) Xiao, D.; Liu, G.-B.; Feng, W.; Xu, X.; Yao, W. Coupled Spin and Valley Physics in Monolayers of MoS₂ and Other Group-VI Dichalcogenides. *Phys. Rev. Lett.* **2012**, *108* (19), 196802.
- (30) Wu, R.; Zhang, H.; Ma, H.; Zhao, B.; Li, W.; Chen, Y.; Liu, J.; Liang, J.; Qin, Q.; Qi, W.; Chen, L.; Li, J.; Li, B.; Duan, X. Synthesis, Modulation, and Application of Two-Dimensional TMD Heterostructures. *Chem. Rev.* **2024**, *124* (17), 10112–10191.
- (31) Shah, S. J.; Chen, J.; Xie, X.; Oyang, X.; Ouyang, F.; Liu, Z.; Wang, J.-T.; He, J.; Liu, Y. Progress and Prospects of Moiré Superlattices in Twisted TMD Heterostructures. *Nano Res.* **2024**, *17* (11), 10134–10161.
- (32) Liu, Y.; Weiss, N. O.; Duan, X.; Cheng, H.-C.; Huang, Y.; Duan, X. Van Der Waals Heterostructures and Devices. *Nat. Rev. Mater.* **2016**, *1* (9), 16042.
- (33) Zimmermann, J. E.; Axt, M.; Mooshammer, F.; Nagler, P.; Schüller, C.; Korn, T.; Höfer, U.; Mette, G. Ultrafast Charge-Transfer Dynamics in Twisted MoS₂/WSe₂ Heterostructures. *ACS Nano* **2021**, *15* (9), 14725–14731.
- (34) Tran, K.; Moody, G.; Wu, F.; Lu, X.; Choi, J.; Kim, K.; Rai, A.; Sanchez, D. A.; Quan, J.; Singh, A.; Embley, J.; Zepeda, A.; Campbell, M.; Autry, T.; Taniguchi, T.; Watanabe, K.; Lu, N.; Banerjee, S. K.; Silverman, K. L.; Kim, S.; Tutuc, E.; Yang, L.; MacDonald, A. H.; Li, X. Evidence for Moiré Excitons in van Der Waals Heterostructures. *Nature* **2019**, *567* (7746), 71–75.
- (35) Wu, R.; Tao, Q.; Li, J.; Li, W.; Chen, Y.; Lu, Z.; Shu, Z.; Zhao, B.; Ma, H.; Zhang, Z.; Yang, X.; Li, B.; Duan, H.; Liao, L.; Liu, Y.; Duan, X.; Duan, X. Bilayer Tungsten Diselenide Transistors with On-State Currents Exceeding 1.5 Milliamperes per Micrometre. *Nat. Electron.* **2022**, *5* (8), 497–504.
- (36) Yang, G.; Yang, Y.; Ma, H.; Mao, X.; Li, C.; Li, J.; Zhang, Q.; Zhang, Z.; Yin, F.; Li, J. Realization of a Half-Metallic State on Bilayer WSe₂ Using Doping Transition Metals (Cr, Mn, Fe, Co, Ni) in Its Interlayer. *Nanotechnology* **2018**, *29* (11), 115201.
- (37) Reyntjens, P. D.; Tiwari, S.; Van de Put, M. L.; Sorée, B.; Vandenberghe, W. G. Magnetic Properties and Critical Behavior of Magnetically Intercalated WSe₂: A Theoretical Study. *2D Mater.* **2021**, *8* (2), 025009.
- (38) Giannozzi, P.; Baroni, S.; Bonini, N.; Calandra, M.; Car, R.; Cavazzoni, C.; Ceresoli, D.; Chiarotti, G. L.; Cococcioni, M.; Dabo, I.; Dal Corso, A.; de Gironcoli, S.; Fabris, S.; Fratesi, G.; Gebauer, R.; Gerstmann, U.; Gouguassis, C.; Kokalj, A.; Lazzeri, M.; Martin-Samos, L.; Marzari, N.; Mauri, F.; Mazzarello, R.; Paolini, S.; Pasquarello, A.; Paulatto, L.; Sbraccia, C.; Scandolo, S.; Sclauzero, G.; Seitsonen, A. P.; Smogunov, A.; Umari, P.; Wentzcovitch, R. M. QUANTUM ESPRESSO: A Modular and Open-Source Software Project for Quantum Simulations of Materials. *J. Phys.: Condens. Matter* **2009**, *21* (39), 395502.
- (39) Perdew, J. P.; Burke, K.; Ernzerhof, M. Generalized Gradient Approximation Made Simple. *Phys. Rev. Lett.* **1996**, *77* (18), 3865–3868.
- (40) Timrov, I.; Marzari, N.; Cococcioni, M. H. P. – A Code for the Calculation of Hubbard Parameters Using Density-Functional Perturbation Theory. *Comput. Phys. Commun.* **2022**, *279*, 108455.
- (41) Monkhorst, H. J.; Pack, J. D. Special Points for Brillouin-Zone Integrations. *Phys. Rev. B* **1976**, *13* (12), 5188–5192.
- (42) Henkelman, G.; Arnaldsson, A.; Jónsson, H. A Fast and Robust Algorithm for Bader Decomposition of Charge Density. *Comput. Mater. Sci.* **2006**, *36* (3), 354–360.
- (43) Tang, W.; Sanville, E.; Henkelman, G. A Grid-Based Bader Analysis Algorithm without Lattice Bias. *J. Phys.: Condens. Matter* **2009**, *21* (8), 084204.
- (44) Sanville, E.; Kenny, S. D.; Smith, R.; Henkelman, G. Improved Grid-based Algorithm for Bader Charge Allocation. *J. Comput. Chem.* **2007**, *28* (5), 899–908.
- (45) Yu, M.; Trinkle, D. R. Accurate and Efficient Algorithm for Bader Charge Integration. *J. Chem. Phys.* **2011**, *134* (6), 1–8.
- (46) Momma, K.; Izumi, F. VESTA 3 for Three-Dimensional Visualization of Crystal, Volumetric and Morphology Data. *J. Appl. Crystallogr.* **2011**, *44* (6), 1272–1276.
- (47) Kokalj, A. XCrySDen-a New Program for Displaying Crystalline Structures and Electron Densities. *J. Mol. Graph. Model.* **1999**, *17* (3–4), 176–179.
- (48) Soulén, R. J.; Byers, J. M.; Osofsky, M. S.; Nadgorny, B.; Ambrose, T.; Cheng, S. F.; Broussard, P. R.; Tanaka, C. T.; Nowak, J.; Moedera, J. S.; Barry, A.; Coey, J. M. D. Measuring the Spin Polarization of a Metal with a Superconducting Point Contact. *Science* **1998**, *282* (5386), 85–88.
- (49) Anderson, P. W. New Approach to the Theory of Superexchange Interactions. *Phys. Rev.* **1959**, *115* (1), 2–13.
- (50) Kanamori, J. Supereexchange Interaction and Symmetry Properties of Electron Orbitals. *J. Phys. Chem. Solids* **1959**, *10* (2–3), 87–98.
- (51) Geertsma, W.; Khomskii, D. Influence of Side Groups on 90° Superechange: A Modification of the Goodenough-Kanamori-Anderson Rules. *Phys. Rev. B* **1996**, *54* (5), 3011–3014.
- (52) Ruderman, M. A.; Kittel, C. Indirect Exchange Coupling of Nuclear Magnetic Moments by Conduction Electrons. *Phys. Rev.* **1954**, *96* (1), 99–102.
- (53) Kasuya, T. A Theory of Metallic Ferro- and Antiferromagnetism on Zener's Model. *Prog. Theor. Phys.* **1956**, *16* (1), 45–57.
- (54) Yosida, K. Magnetic Properties of Cu-Mn Alloys. *Phys. Rev.* **1957**, *106* (5), 893–898.
- (55) Xue, Y.; Shen, Z.; Wu, Z.; Song, C. Theoretical Prediction of Curie Temperature in Two-Dimensional Ferromagnetic Monolayer. *J. Appl. Phys.* **2022**, *132* (5), 1–10.
- (56) Tiwari, S.; Van de Put, M. L.; Sorée, B.; Vandenberghe, W. G. Magnetic Order and Critical Temperature of Substitutionally Doped Transition Metal Dichalcogenide Monolayers. *npj 2D Mater. Appl.* **2021**, *5* (1), 54.
- (57) Anderson, P. W. Antiferromagnetism Theory of Superechange Interaction. *Phys. Rev.* **1950**, *79* (2), 350–356.
- (58) Wu, M.; Yao, X.; Hao, Y.; Dong, H.; Cheng, Y.; Liu, H.; Lu, F.; Wang, W.; Cho, K.; Wang, W.-H. Electronic Structures, Magnetic Properties and Band Alignments of 3d Transition Metal Atoms Doped Monolayer MoS₂. *Phys. Lett. A* **2018**, *382* (2–3), 111–115.